



Analysis of Elements Non-Uniform Distribution of FeCoCrNi High-Entropy Alloy Coatings on Ti–6Al–4V Surface by Laser Cladding

Shuyao Duan¹ · Xiaohong Zhan² · Mengyao Wu¹ · Hengchang Bu¹ · Qiyu Gao³

Received: 22 July 2020 / Accepted: 13 October 2020 / Published online: 2 January 2021
© The Korean Institute of Metals and Materials 2021

Abstract

The evolution of element distribution during laser cladding involves two dynamic behaviors, i.e., liquid molten pool flow and FeCoCrNi high-entropy alloy (HEA) coatings solidification. However, it is quite difficult to characterize element distribution during the flow of the liquid molten pool rigorously. The current investigation conducted the optical microscopy, scanning electron microscopy, X-ray diffraction analysis and energy dispersive spectrometer to study the dilution, phase composition, microstructure of the FeCoCrNi coatings. The flow field was simulated to uncover the dynamic change mechanism of the molten pool and explain the experimental results. The results indicated that the coating is substantially composed of FCC and BCC solid solution with a typical dendrite microstructure. Gray Laves phase-(Ni, Co)₂Ti and a small number of white dot particles, Fe–Cr phase, are dispersed in the inter-dendritic region. The HEA atoms (Fe, Co, Cr, Ni) gradually aggregate from the center to the side at the coating boundary region, while the Ti atom is the opposite. The Marangoni flow inflection point at the molten pool boundary will cause HEA atoms to aggregate. On the contrary, Ti atom enters the molten pool from the bottom with the heat buoyance flow and then migrates to the boundary along with the Marangoni flow. Therefore, the content of Ti in the coating boundary decreases. The Marangoni flow, heat buoyance flow, and recoil pressure flow are interwoven in the middle region of the coating, resulting in a more uniform element distribution than the boundary region.

Keywords Ti–6Al–4V · Laser cladding · High-entropy alloy coatings · Microstructure · Element distribution · Molten pool flow

1 Introduction

Ti–6Al–4V is one of the significant materials for the aerospace industry because of its high specific strength, excellent corrosion resistance and toughness properties compared to other structural materials [1]. Nevertheless, the high friction coefficient and low hardness that are confined to obtain excellent surface performance have restricted the widespread application of titanium alloys [2, 3]. The surface

modification technology such as laser cladding is a promising way to repair and strengthen material surfaces. The high energy density of the laser results in a coating thickness that is adjustable (from micrometers to several millimeters) and maintains a strong metallurgical bond to the substrate [4–6].

The literature abounds with correlation studies of the laser cladding. Given the category of powder material according to the selection and ratio of the cladding material. The most commonly investigated powder material are Ni-based alloys [7], Fe-based alloy [8], Co-based alloy [9], intermetallic compounds Ti–Al [10], Fe–Al [11], Ti–Ni [12], Ni–Al [13], ceramic phases TiN [14], TiB [15], TiC [16], Ti₅Si₃ [17], Al₂O₃ [18] and composite coatings [19, 20]. High entropy alloys (HEAs), proposed by Yeh et al. [21] in 2004, is a new concept in alloy design, which is made up of more than five metallic elements in equimolar or near-equimolar ratios. High entropy alloys exhibit uniqueness as they are usually composed of simple solid solutions with a BCC structure [22] or FCC [23] structure. High-entropy alloys (HEA) possess special and expected properties such as high

✉ Xiaohong Zhan
xiaohongzhan_nuaa@126.com

¹ College of Material Science and Technology, Nanjing University of Aeronautics and Astronautics, Nanjing 211106, China

² National Key Laboratory of Science and Technology on Helicopter Transmission, Nanjing University of Aeronautics and Astronautics, Nanjing 211106, China

³ College of Science, Nanjing University of Aeronautics and Astronautics, Nanjing 211106, China

hardness and wear resistance by means of the appropriate selection of the alloying elements. Consequently, HEAs are considered as a promising coating material for improving the surface performance of titanium alloys.

Most of the research conducted so far on the fabrication of high entropy alloys by laser cladding technology focused on the following three aspects: the design of HEAs elements, microstructural evolution [24], and the improvement in properties, which include microhardness [25], wear resistance [26], corrosion resistance [27], high-temperature oxidation resistance [28]. Elemental segregation during the coating solidification was discovered for the reason that HEAs consist of multiple elements and each element exhibits different properties. Yue et al. [29] investigated the solidification behavior of AlCoCrCuFeNi HEAs on magnesium substrates. The simulation results indicated that some Cu elements diffuse into the Mg melt and subsequently solidifies following the Mg–Cu phase diagram due to the lower affinity of Cu elements to other HEA elements. Guo et al. [30] proposed the viewpoint that high melting point elements accumulate in the region of primary solidification and low melting point elements accumulate in the region of final solidification.

Elemental segregation during solidification is generally caused by the difference in element properties. The laser-powder/substrate interaction causes the coating powder to be melted before the molten pool solidifies. The liquid coating produces a violent flow under the effect of surface tension, thermal buoyancy and steam recoil pressure, resulting in matrix Ti atoms and HEA elements disperse to the various area of the molten pool [31]. The difference of flow direction and velocity in different regions leads to the uneven distribution of elements in liquid coating and the change of microstructure evolution during solidification, which ultimately

affects the surface properties of HEAs coating. Therefore, it is necessary to explore the influence of molten pool flow on element distribution in laser cladding HEAs coating.

In the present investigation, the FeCoCrNi alloy powder was used to fabricate HEAs coatings on Ti–6Al–4V (TC4) titanium alloy by laser cladding. The dilution rate of the coatings with different heat input and preplaced layer thickness were investigated. Furthermore, the microstructure characteristics are explained according to the aggregation of Ti atoms. The distribution characteristics of HEAs elements (FeCoCrNi) and matrix Ti atoms in the upper boundary region, the lower boundary region and the middle region of the coating were interpreted according to the convection characteristics. The flow field was simulated to uncover the dynamic change mechanism of the molten pool and explain the experimental results.

2 Experimental Details

140×70×6 mm TC4 titanium alloy was applied as the substrate for laser cladding in this study. The TC4 matrix at normal temperature exhibits a stable $\alpha + \beta$ phase, which is shown in Fig. 1a. In addition, the FeCoCrNi HEAs powder used in the experiment is prepared by vacuum gas atomization with a size of 15–53 μm (Fig. 1b). And the chemical composition of TC4 substrate and FeCoCrNi HEAs powder is detailed presented in Table 1.

In order to avoid the introduction of extra impurities in the binder, the pre-set powder method was applied in the experiment. Moreover, two grooves with depths of 0.5 mm and 1 mm were cut on the substrate to improve the accuracy of preplaced powder thickness. Then the powder was

Fig. 1 Morphology of TC4 matrix and FeCoCrNi HEAs powder in laser cladding experiment

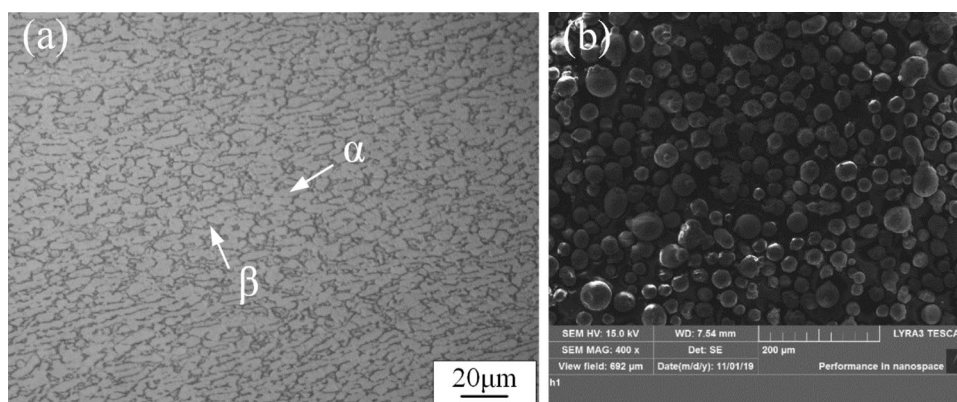


Table 1 Chemical composition of TC4 titanium alloy and FeCoCrNi HEAs powder

Chemical composition (wt%)	Fe	Co	Cr	Ni	Ti	Al	V
Ti–6Al–4V	≤0.15	0	0	0	Bal.	6.04	3.71
FeCoCrNi HEA power	24.44	26.18	22.43	Bal.	0	0	0

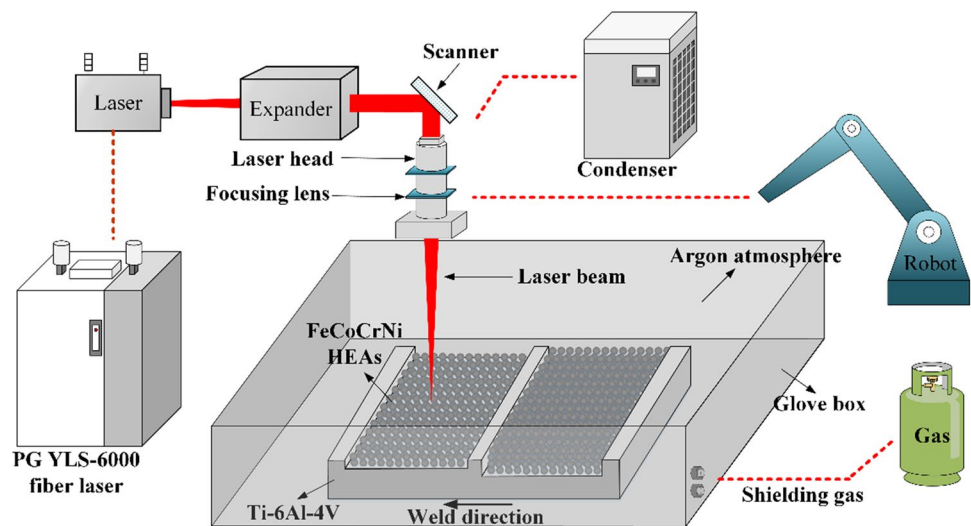
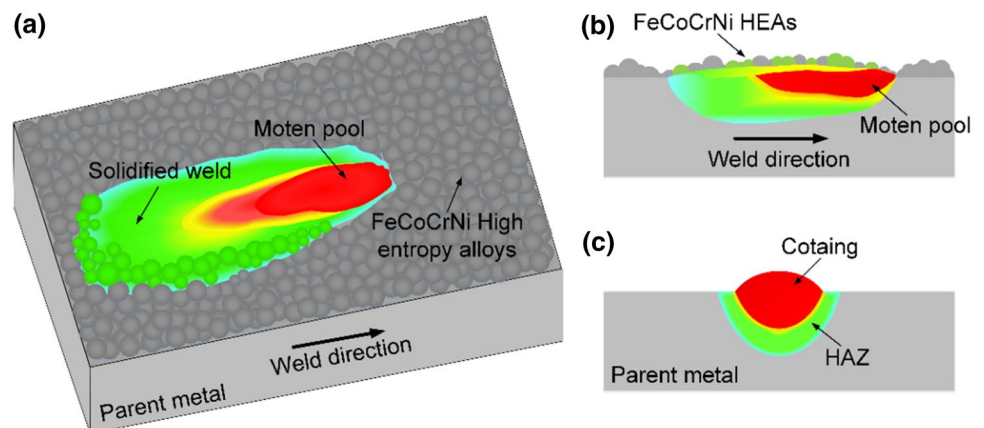
Table 2 The experiment parameters of laser cladding FeCoCrNi HEAs coatings

Series	Case	Laser power (W)	Scanning speed (mm/s)	Heat input (J/mm ²)	Powder thickness (mm)
1	1	800	12	33.3	0.5
	2	800	10	40	
	3	1200	12	50	
	4	1000	8	62.5	
	5	1200	8	75	
2	6	800	12	33.3	1
	7	800	10	40	
	8	1200	12	50	
	9	1000	8	62.5	
	10	1200	8	75	

spread evenly on the surface of the substrate and compacted to ensure the coating thickness is equal to the groove height.

The experiment was conducted in a glove box filled with argon shielding gas, which contained less than 60 ppm of oxygen to prevent the molten metal from oxidizing. A 6-axis KUKA robot was used to operate the laser cladding process, which was equipped with a Rofin-Sinar laser system capable of achieving the power of 2000 W. Before laser cladding, the substrate surface was polished with a grinding wheel to improve the surface finish, subsequently, cleaned with ethanol. All final coatings were fabricated with the basic parameters, which were given in Table 2. Besides, the focal length employed in each experiment is 60 mm uniformly. The laser cladding system is displayed in Fig. 2. And a schematic view of the laser cladding process is depicted in Fig. 3.

The metallographic samples along the cross-section of specimens were observed by optical microscopy after chemically etching in Keller reagent (consisting of 2.5% HNO₃ + 1.5% HCl + 1% HF + 95% H₂O). The phase identification was measured by an Empyrean XRD system. And the microstructure of the coatings was observed using a scanning electron microscope. Quantitative distribution results

Fig. 2 Diagrammatic sketch and experimental apparatus of laser cladding**Fig. 3** Schematic diagram of laser cladding process. **a** 3D view; **b** vertical-sectional view; **c** cross-sectional view

of major alloy elements in the coatings were investigated via EDS analysis.

3 Numerical Methods

3.1 Heat Transfer and Fluid Flow in the Laser Cladding

A three-dimensional steady-state model was established, while the heat transfer and fluid flow in the molten pool were calculated by solving the equations for the conservation of energy, momentum and mass. Since the coating is symmetrical about the centerline only half of the workpiece is considered in the calculations. The molten metal is assumed to be an incompressible, laminar, and Newtonian fluid. The substrate with dimensions of $50 \times 10 \times 8$ mm was established, while the morphology of the coating was consistent with the experimental results. The finite element mesh was exhibited in Fig. 4a.

Since the temperature of the materials in the laser cladding process change rapidly, it is necessary to define the thermal physical properties of the substrate and the FeCoCrNi HEAs powder at different temperatures to obtain accurate simulation results. In this paper, the specific heat, thermal conductivity, viscosity and surface tension is varied with temperature, while density is defined as constant. Furthermore, the effect of the latent heat of fusion is considered.

3.2 The Initial and Boundary Condition

The initial condition refers to ambient temperature of the workpiece, which can be set to 20°C since the actual laser cladding process is conducted at room temperature. And the boundary condition refers to the heat convection of the parent metals at ambient temperature. As the cooling

medium has a significant influence on the temperature field and microstructure of the FeCoCrNi HEAs coating [32], it is critical to define the correct convective heat transfer coefficient, which is determined by the cooling medium. The convective heat transfer coefficient is set to be $40 \text{ [J/(m}^2 \text{ K)]}$ since air is the cooling medium in this research [33], while the boundary convection condition is applied to all external surfaces of the finite element model.

In this paper, due to the low laser power and fast scanning speed, the keyhole effect will not appear in the laser experiment, and the ratio of depth to width is small. Therefore, the Gaussian surface heat source model is used to characterize the thermal effect in laser cladding, as displayed in Fig. 4b.

4 Results and Discussion

4.1 Macromorphology and Dilution Rate

Figure 5 illustrated the cross-sectional profiles of the samples, which can be divided into three zones: substrate, heat-affected zone (HAZ), and coating. The arched surface of the coating is located above the substrate and the fused line can be observed between HAZ and the coating, demonstrating a good metallurgical bonding is formed. Dilution rate η can be calculated as follows [34]:

$$\eta = \frac{S_1}{S_1 + S_2} \quad (1)$$

where S_1 is the fusion area of the substrate and S_2 is the area of the coating above the substrate surface.

The cross-sectional morphology of the coating can be considered as a combination of two ideal arcs with different radii. W_1 is the width of the approximate arc of the molten substrate and W_2 is the maximum width of the coating.

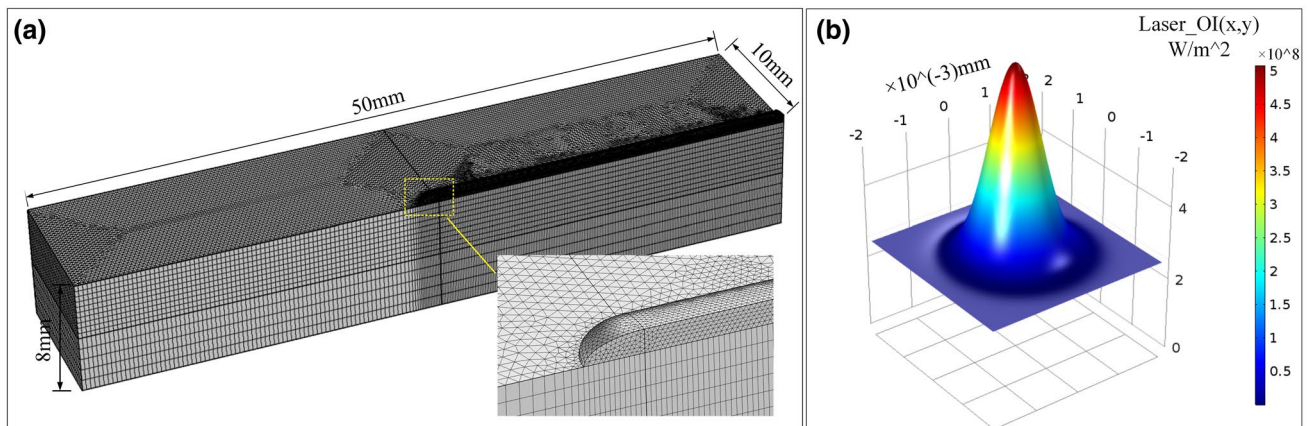
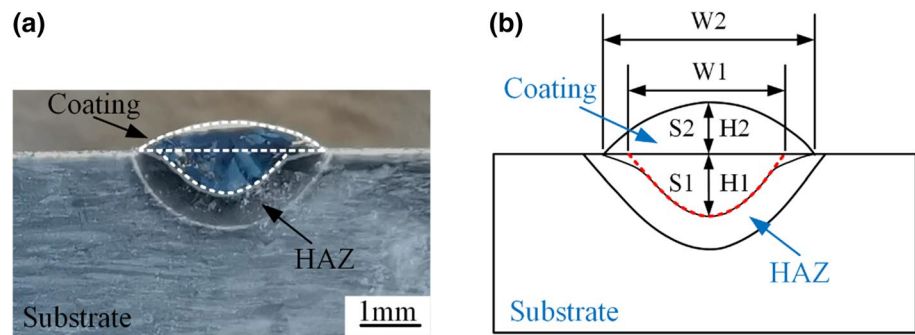


Fig. 4 Geometric and heat source model. **a** Geometric model; **b** Gaussian heat source model

Fig. 5 Morphology of cross-section of the coating. **a** SEM image; **b** geometric models for calculating the dilution rate of the coating



While, H_1 and H_2 are the depth of the molten substrate and height of the coating above the surface of the substrate, respectively. S_1 and S_2 can be calculated by a geometric relation as follows [14]:

$$S_1 = \left\{ \frac{\left[\left(\frac{W_1}{2} \right)^2 + H_1^2 \right]^2}{2H_1} \right\} \times \arcsin \left\{ \frac{W_1 \cdot H_1}{\left[H_1^2 + \left(\frac{W_1}{2} \right)^2 \right]} \right\} - \frac{W_1 \left[\left(\frac{W_1}{2} \right)^2 - H_1^2 \right]}{4H_1} \quad (2)$$

$$S_2 = \left\{ \frac{\left[\left(\frac{W_2}{2} \right)^2 + H_2^2 \right]^2}{2H_2} \right\} \times \arcsin \left\{ \frac{W_2 \cdot H_2}{\left[H_2^2 + \left(\frac{W_2}{2} \right)^2 \right]} \right\} - \frac{W_2 \left[\left(\frac{W_2}{2} \right)^2 - H_2^2 \right]}{4H_2} \quad (3)$$

When the cladding material is radiated by the laser beam, one part of the energy is reflected and absorbed by the cladding material, the remainder is applied to the substrate for the formation of the dilution zone. Figure 6 exhibits the variation of W , H , and dilution rate η of the coatings with different heat input and thickness of the preplaced layer.

When the heat input is 33.3 J/mm^2 , the energy is too low to melt the HEAs powder completely, resulting in the H_2 is much lower than the thickness of the preplaced layer both in Series 1 and 2. With the increase of the heat input, the HEAs powder melts completely and the substrate absorbs more energy, which leads to a constantly improved H_1 . Similarly, W_1 and W_2 increase with the expansion of the molten pool. However, the initial thickness of the preplaced layer determines the upper limit of H_2 . And when the molten pool expands, the upper surface of the molten pool tends to be smoother under the action of gravity, which causes a slight decrease in H_2 . For Series 2 (powder thickness: 1 mm), the area of S_2 is larger due to the thicker preplaced layer, resulting in a significant decrease in H_2 with the increase of heat input (Fig. 6d). When the heat input is 75 J/mm^2 , H_2 of

Series 2 is only 0.84 mm, which is obviously less than the thickness of the preplaced powder layer. On the contrary, the H_2 of Series 1 tends to be stable when the heat input gradually increases (Fig. 6b). Therefore, the thickness of the pre-

placed layer of Series 1 (powder thickness: 0.5 mm) is more reasonable. Furthermore, according to formulas 2 and 3, the circular arc area is determined by W and H . Consequently, the dilution ratio declines previously and increases later as the heat input raises. Case 2 has the lowest dilution ratio of 33.95% when the thickness of the preplaced layer is 0.5 mm.

4.2 Microstructural Characterization

The microstructure of the coating was observed by SEM, and a special region was found in Case 2, which appeared nucleation zone and dendrite zone. In order to realize the phase composition, the FeCoCrNi HEA powder and the coating of Case 2 were analyzed by XRD, which is shown in Fig. 7. The HEAs powder consists of only a single face-centered cubic (FCC), while the HEAs coating of Case 2 mainly contains two simple solid solutions, FCC and body-centered cubic (BCC). The reason is that the addition of Ti element in the matrix changes the valence electron concentration (VEC) of the alloy, inhibiting the formation of FCC phase in the HEAs coating. Guo et al. [35] proposed that FCC phases

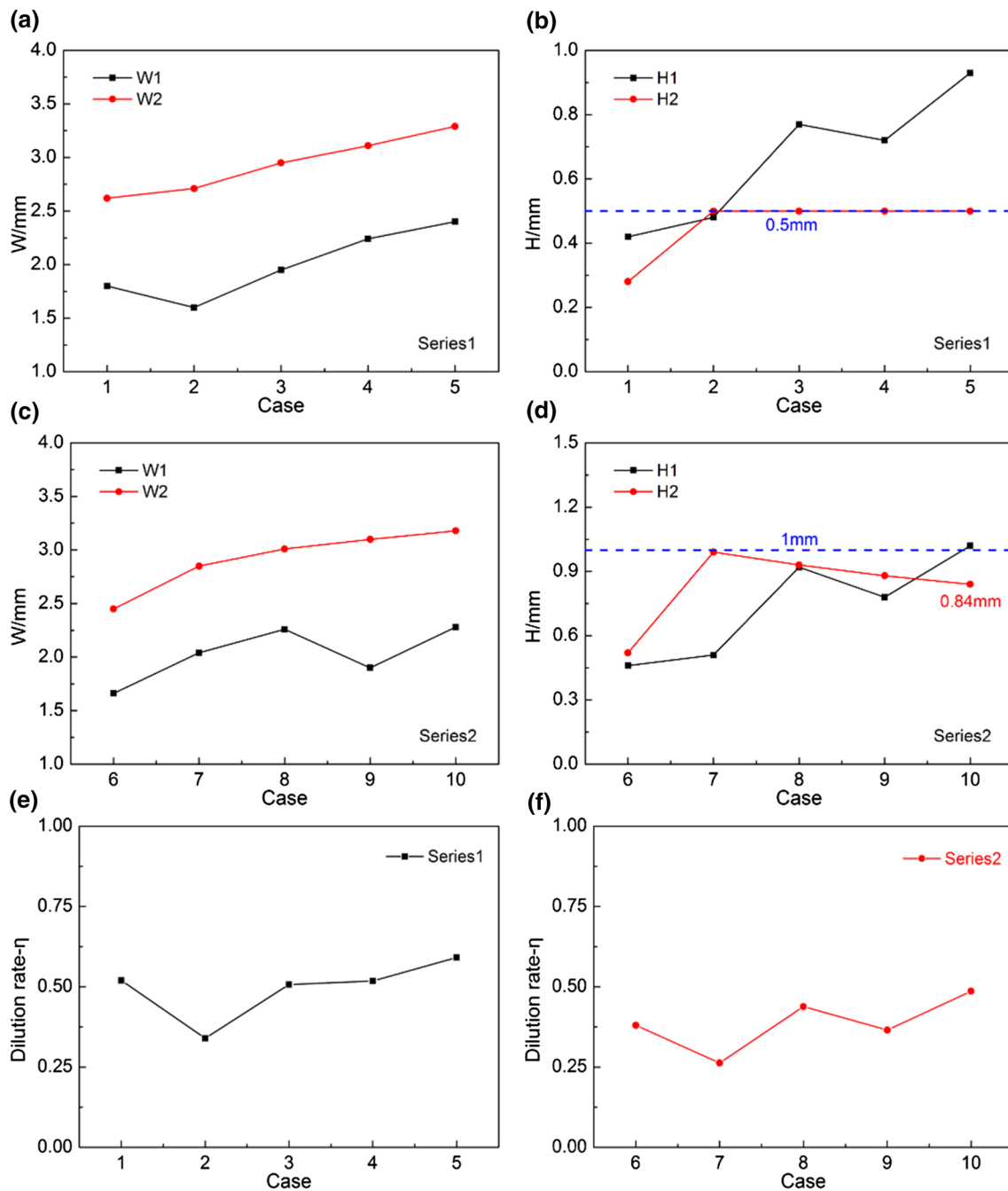


Fig. 6 The change in dilution rate of the coatings with different heat input and thickness of the preplaced layer. **a** W1 and W2 in Series1; **b** H1 and H2 in Series1; **c** W1 and W2 in Series2; **d** H1 and H2 in Series2; **e** dilution rate in Series1; **f** dilution rate in Series2

are stable at higher VEC (≥ 8) and instead BCC phases are stable at lower VEC (< 6.87). Since the VEC of Ti element is 4, it promotes the transition from FCC structure to BCC structure. Besides, Jan Schroers [36] reveals that HEAs with increasing atomic size difference prefer BCC structure over FCC due to the ability of the BCC structure to accommodate a large atomic size divergence with lower strain energy penalty. The atomic size of Ti element is quite different from that of HEA powder (Fe, Co, Cr, Ni), which is beneficial to

the formation of BCC phase in coatings. Moreover, Fe–Cr phase and Laves phase were found in the coating.

Figure 8 represents the microstructure of the nucleation and dendrite zone in the coating of Case 2. The nucleation region is mainly composed of gray phase-A and white dendritic crystal-B. Nevertheless, the gray phase in the dendrite area is significantly reduced and the white dendritic crystal greatly increases. Meanwhile, some white dot particles-C are precipitated on the edge of the dendritic crystal. Cieslak

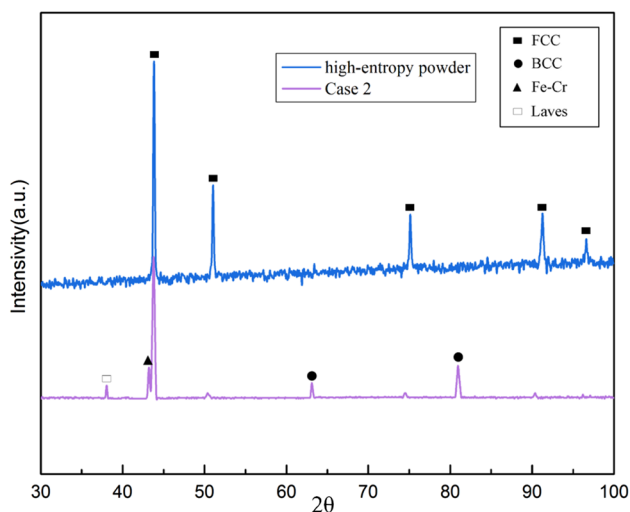


Fig. 7 XRD patterns of FeCoCrNi HEAs powder and Case 2

et al. [37] observed the phase are dark or bright, with a dendritic structure, during preparing HEA coatings of similar composition. And analogous microstructure has been already reported in other studies [38, 39].

Then, the phase composition of nucleation and dendrite zone in Case 2 was determined by XRD and EDS analysis. EDS results are presented in Table 3. The main elements of gray phase-A are Ni, Co and Ti elements. Ti and Ni, Ti and Co have the largest negative ΔH_{mix} , which decreases the Gibbs energy of the (Ni, Co, Ti)-rich phase.

$$\Delta G_{mix} = \Delta H_{mix} - T\Delta S_{mix} \tag{4}$$

where G_{mix} is the Gibbs energy, H_{mix} is the enthalpy, S_{mix} is the entropy and T is the absolute temperature [40]. Therefore, the gray phase-A is (Ni, Co)₂Ti-Laves phase. Moreover, the white dendritic crystal-B is BCC + FCC solid solution structure, whose content of Fe and Cr improves apparently, while Ni and Co reduce, which has been already reported in other researches [37].

Furthermore, the gray phase-A in nucleation area is much more than that in dendrite area. It can be known from the

Fig. 8 The microstructure of the nucleation and dendrite zone in the coating of Case 2. **a** macro-morphology; **b** microstructure of the special area; **c** magnified microstructure of nucleation zone; **d** Magnified microstructure of dendrite zone

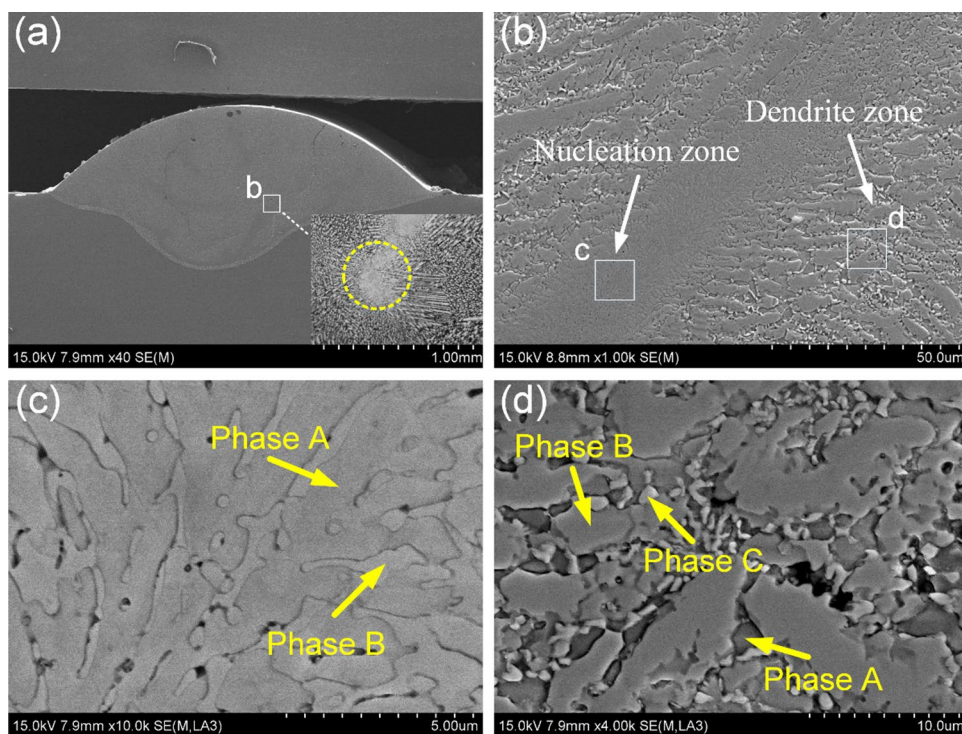


Table 3 Elements concentration in different microstructure of the nucleation and dendrite zone

Region	Phase	Ti (wt%)	Al (wt%)	V (wt%)	Fe (wt%)	Co (wt%)	Cr (wt%)	Ni (wt%)
Nucleation zone	A	35.18	3.21	1.15	12.13	19.15	6.50	22.48
	B	35.42	3.34	1.66	14.88	13.35	13.88	17.46
Dendrite zone	A	26.58	3.70	1.77	12.39	20.54	13.46	21.56
	B	28.60	1.77	0.56	20.19	17.59	17.86	12.71
	C	12.76	1.69	3.51	20.09	11.16	39.48	11.31

above that Ti is the key element for the formation of the gray phase-A. Then, comparing the concentration of Ti, nucleation zone is significantly greater than that in dendrite zone. It is proved that the Ti elements in the matrix was melt and brought into the coating under the agitation of the molten pool, but due to the high heating and cooling rates of the laser cladding process, it is difficult for Ti atoms to distribute uniformly in the coating. Consequently, it is easy to form (Ni, Co, Ti)-rich phase in the region where Ti elements gather. And white dendritic crystal is formed with FCC and BCC solid solution structure along the edge of nucleation area. As the solubility of Fe and Cr reaches the limit, white dot particles-C (Fe–Cr phase) will precipitate out of the dendrites.

The microstructure of the upper, middle and lower parts of the coating in Case 2 is exhibited in Fig. 9, which are all composed of a large number of white dendritic crystals, a small amount of gray phase and white dot particles. Combined with Fig. 8, Laves-phase dominates in the nucleation zone where Ti elements gather. But in general, the coating is mainly composed of white dendritic crystals (FCC + BCC) and a few Fe–Cr phases precipitate out of the dendrites, which is consistent with the XRD results. In addition, since the large amount of energy absorbed by the upper part of the coating, the dendritic crystals gradually coarsen from the bottom to the top. Moreover, the effect of the thickness of the prepared layer on the microstructure of the coating under the same heat input (40 J/mm^2) is delineated in Fig. 10. When the thickness is 1 mm, the size of the microstructure

is extremely uneven and a large number of coarse grains appear. The result is likely to be attributed to the non-equilibrium process with high heating and cooling rate in laser cladding. As the thickness increasing, the molten pool will expand, which will further reduce the uniformity of the coating microstructure. Therefore, the microstructure of the coating is more uniform with a 0.5 mm thickness of the prepared layer.

4.3 Effect of Molten Pool Flow on Element Distribution of the Coating

During the laser cladding process, the HEA powder and substrate are melt into liquid, the molten pool is coupled by various forces, which will produce strong convection. The simulation results of three-dimensional flow in the molten pool are shown in Fig. 11. Specifically, the major driving forces including the recoil pressure, surface tension, and heat buoyance, as elucidated in Fig. 12.

Figure 12a reveals that the surface temperatures below the laser spot can easily reach boiling values. The vapor recoil pressure adds extra forces to the surface of the liquid, which creating a depression of the molten pool surface below the laser, even a keyhole [41]. Therefore, the local liquid metal flows downwards to the bottom at the depression.

Next in Fig. 12b, the strong temperature gradients below the laser necessitate enabling temperature-dependent surface tension.

Fig. 9 The microstructure of the upper, middle and lower parts of the coating in Case 2. **a** macro-morphology; **b** upper; **c** middle; **d** lower

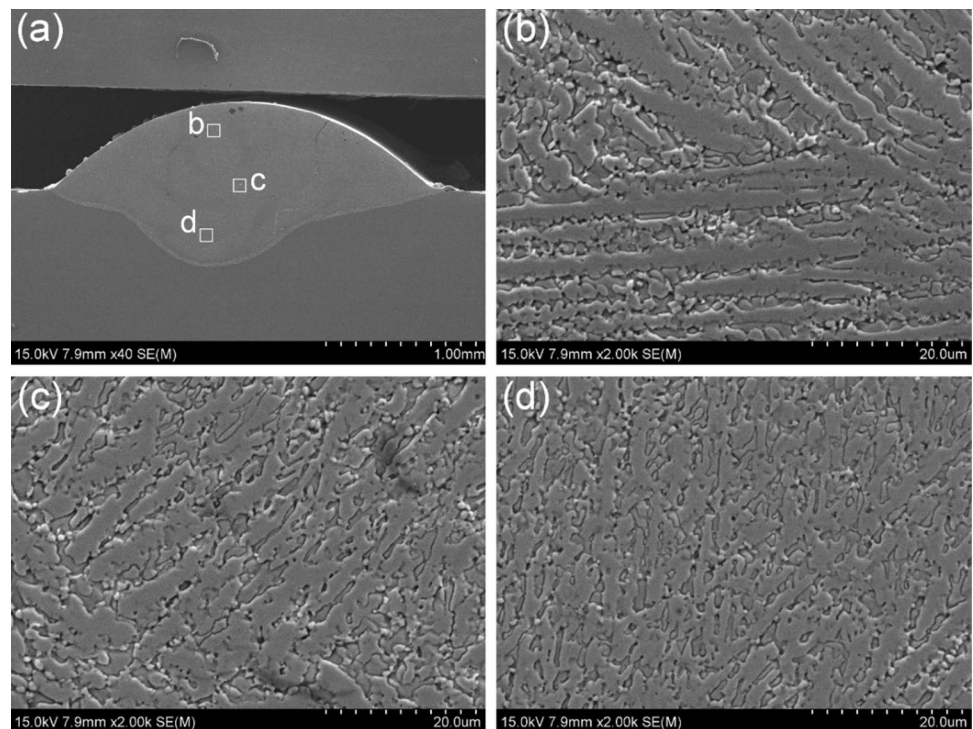


Fig. 10 The microstructure of the coating under the same heat input (40 J/mm²). **a** Case2; **b** Case7

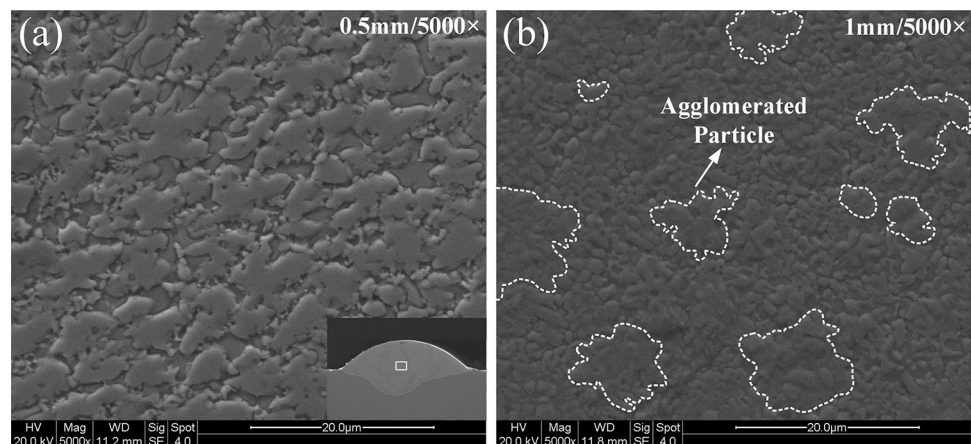
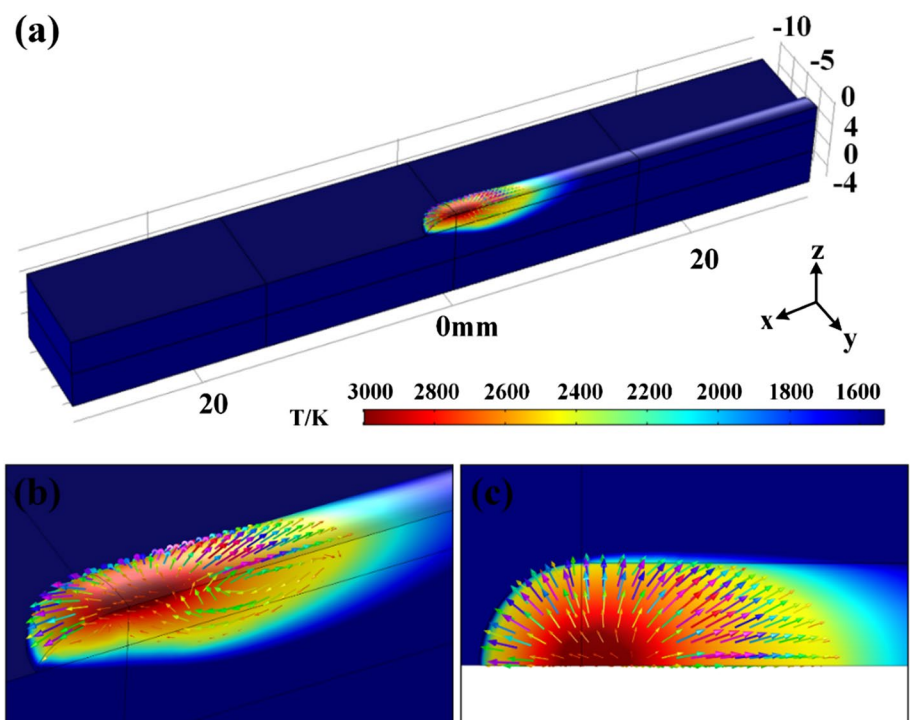


Fig. 11 The simulation results of three-dimensional flow in the molten pool. **a** calculation results of temperature and flow field in the molten pool; **b** partial magnification of the molten pool; **c** vertical view



$$\sigma(T) = 3.282 - 8.9e^{-4}T \quad (5)$$

where T is the temperature in Kelvin. This creates Marangoni effects. It drives the liquid metal from the hot laser spot toward the cold rear [42].

Another driving force is heat buoyancy which is given below [43]:

$$f_b = -\rho g \beta (T - T_m) \quad (6)$$

where ρ is the density of the molten metal, g is the gravitation vector, β is the coefficient of thermal expansion and T_m is the melting point.

At the bottom of the coating, the Ti element in the matrix melts and enters into the molten pool. However, the density of Ti is far less than that of HEA atoms (Fe, Co, Cr, Ni), causing buoyancy convection between the bottom of the molten pool and the center, which is indicated in Fig. 12c.

The coating is divided into three regions: boundary zone (upper, lower) and middle zone. EDS analysis is carried out to explore the divergence of element distribution in different regions of the coating. EDS results in the boundary zone (upper, lower) are noticed in Figs. 13 and 14. Case 2 has the lowest dilution rate and the ratio of each element is more uniform. As for Case 3-Case 5,

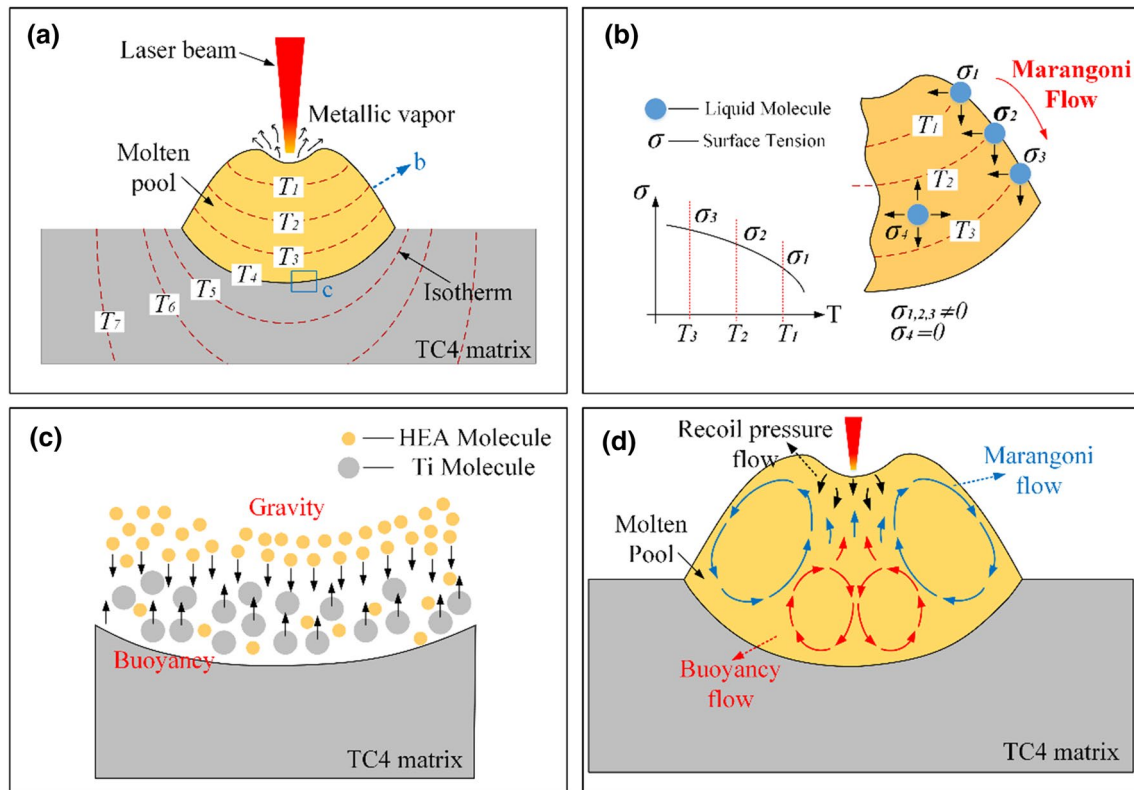


Fig. 12 Flow behavior of molten pool during laser cladding of HEAs. **a** recoil pressure; **b** surface tension; **c** buoyancy convection; **d** flow behavior of the molten pool

due to excessive heat input, high dilution rate, the concentration of Ti atoms enhances obviously. Moreover, an inflection point of the Marangoni flow in the boundary of the molten pool will cause the aggregation of HEA atoms (Fig. 15). Therefore, the content of HEAs elements increases gradually from the center to the side in the boundary zone, which is presented in Figs. 13b–d and 14b–d. On the contrary, Ti enters the molten pool from the bottom with the heat buoyancy flow and then migrates to the boundary of the molten pool along with the Marangoni flow (Fig. 15). Therefore, the content of Ti in coating boundary decreases, as shown in Figs. 13a and 14a.

For the middle zone of the coating, Marangoni flow, heat buoyancy flow and recoil pressure flow are interwoven so that the element distribution in middle zone is more uniform than boundary zone, as illustrated in Fig. 16. Comparing the distribution of elements under

different heat input, no matter boundary zone or middle zone of the coating, HEA atoms show a gradual reduction, while the Ti element increases gradually. The reason is that the augment in heat input leads to a higher dilution rate, which makes more Ti elements enter the molten pool.

5 Conclusion

- (1) For the preplaced layer of 1 mm thickness, the height of the coating decreases significantly with the increase of heat input, the height is unstable, which indicates that 0.5 mm thickness of the preplaced layer is more reasonable. Based on 0.5 mm thickness, Case 2 has the lowest dilution rate of 33.95%.

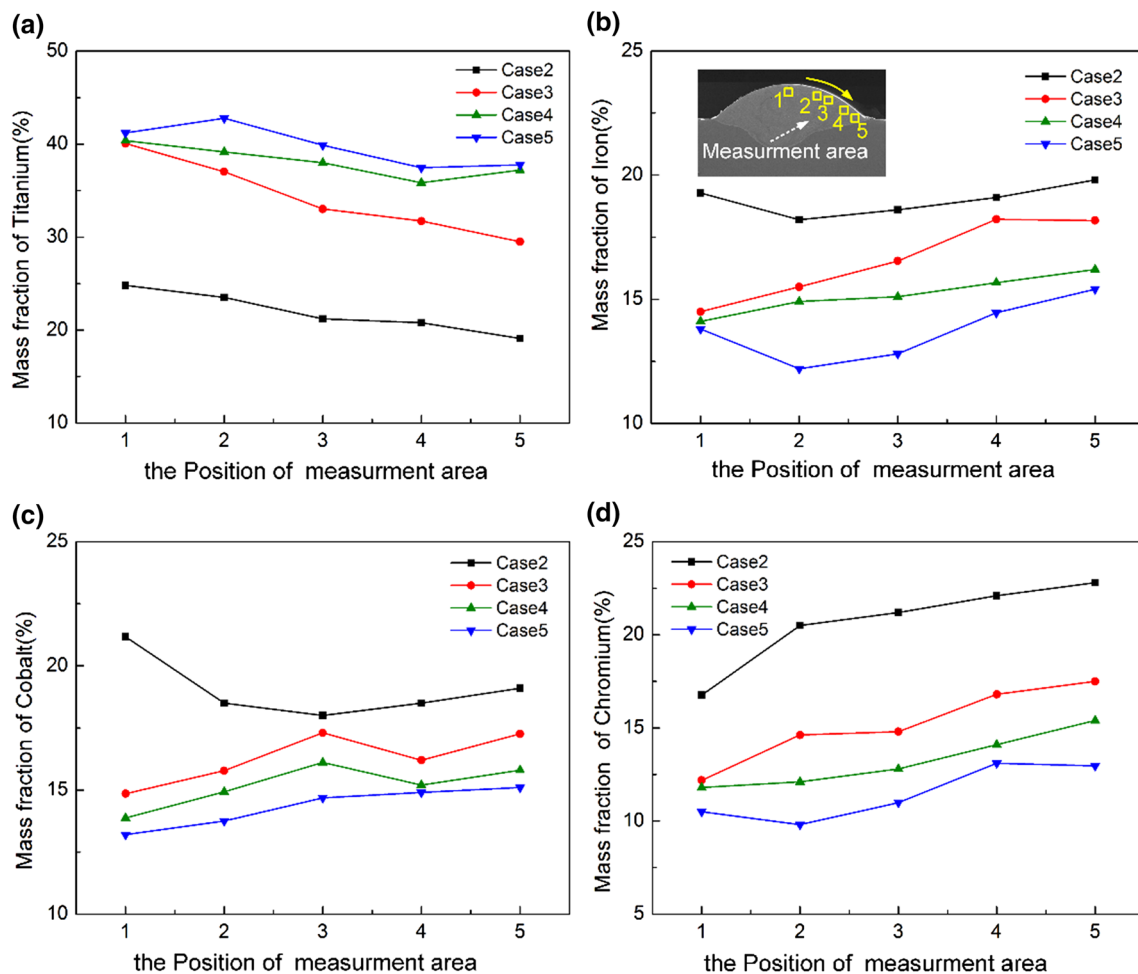


Fig. 13 The element distribution of boundary zone (upper) in the coating. **a** titanium; **b** iron; **c** cobalt; **d** chromium

- (2) The microstructure of FeCoCrNi HEA coating substantially consists of FCC + BCC, which has a typical dendrite structure. The gray Laves phase-(Ni, Co)₂Ti and a small number of white dot particles, Fe–Cr phase, are dispersed in the inter-dendritic region. While, in the region where Ti elements gather, Laves phase dominates, forming a specific nucleation zone, and the dendritic crystal grows along the nucleation zone due to Ti and Ni, Ti and Co have the largest negative ΔH_{mix} .
- (3) The element distribution of the coating is analyzed by EDS. For the boundary zone of the coating, the results show that HEA atoms (Fe, Co, Cr, Ni) gather gradually

- from the center to the side due to an inflection point of the Marangoni flow. On the contrary, Ti enters the molten pool from the bottom with the heat buoyancy flow and then migrates to the boundary along with the Marangoni flow. Therefore, in the boundary zone, the concentration of Ti gradually decreases from the center to the side.
- (4) For the middle zone of the coating, Marangoni flow, heat buoyancy flow and recoil pressure flow are interwoven so that the element distribution is more uniform than the boundary zone.

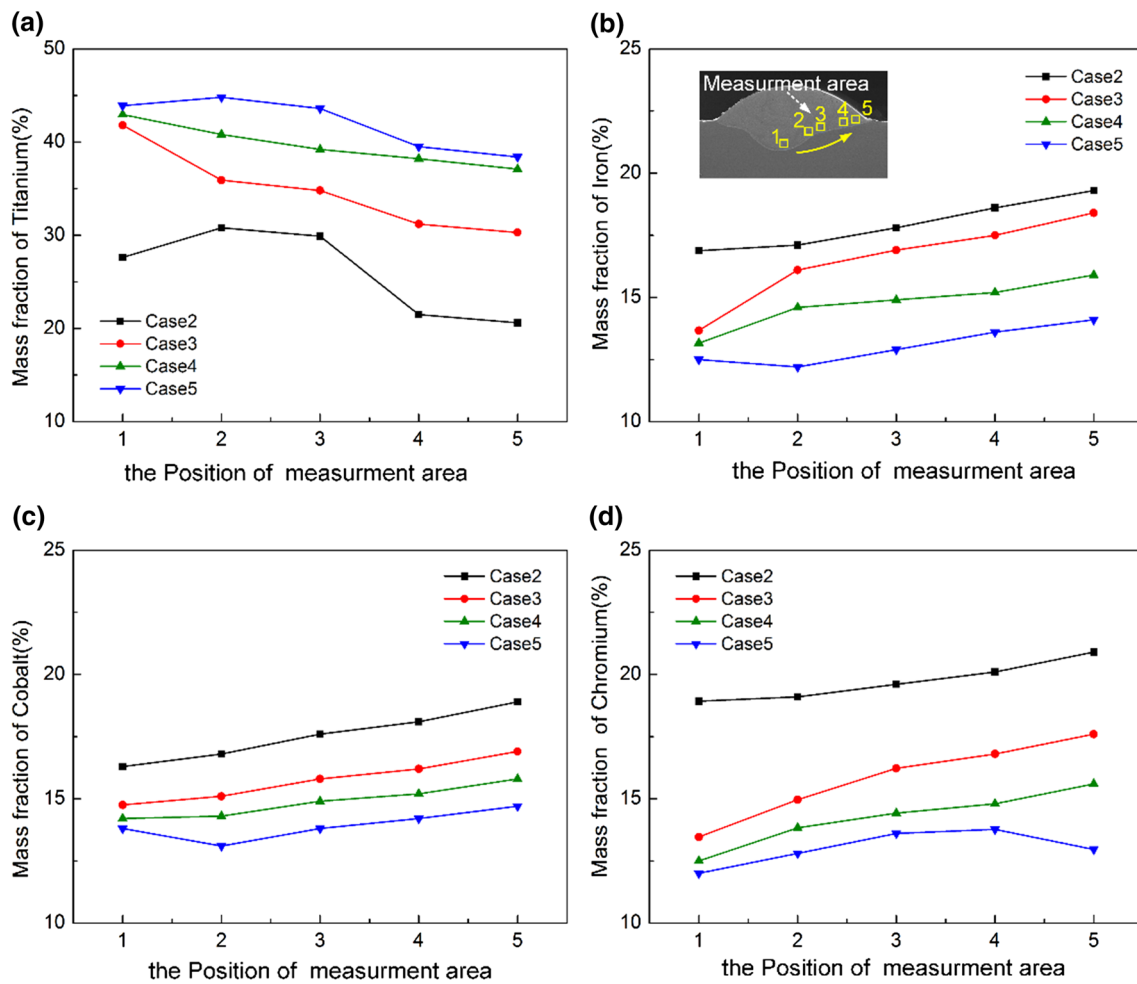


Fig. 14 The element distribution of boundary zone (lower) in the coating. **a** titanium; **b** iron; **c** cobalt; **d** chromium

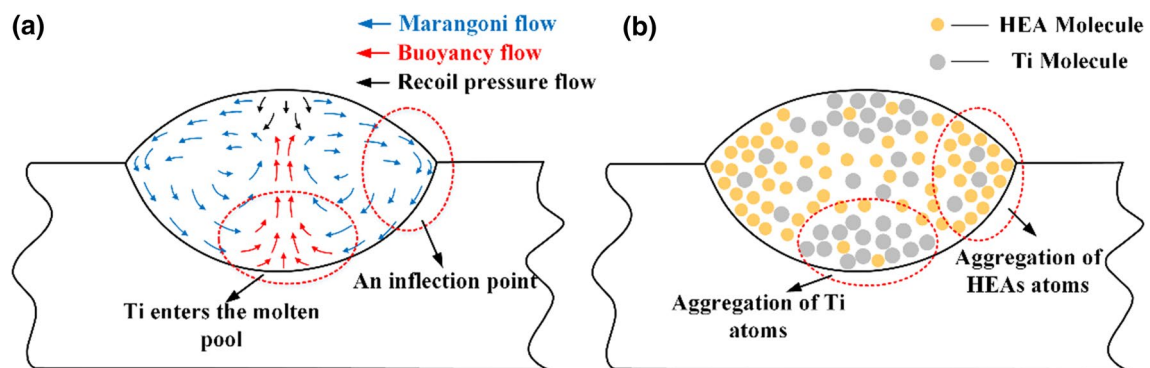


Fig. 15 Schematic diagram of element distribution difference in boundary zone. **a** flow behavior at the bottom and boundary of the molten pool; **b** distribution differences between HEA and Ti atoms

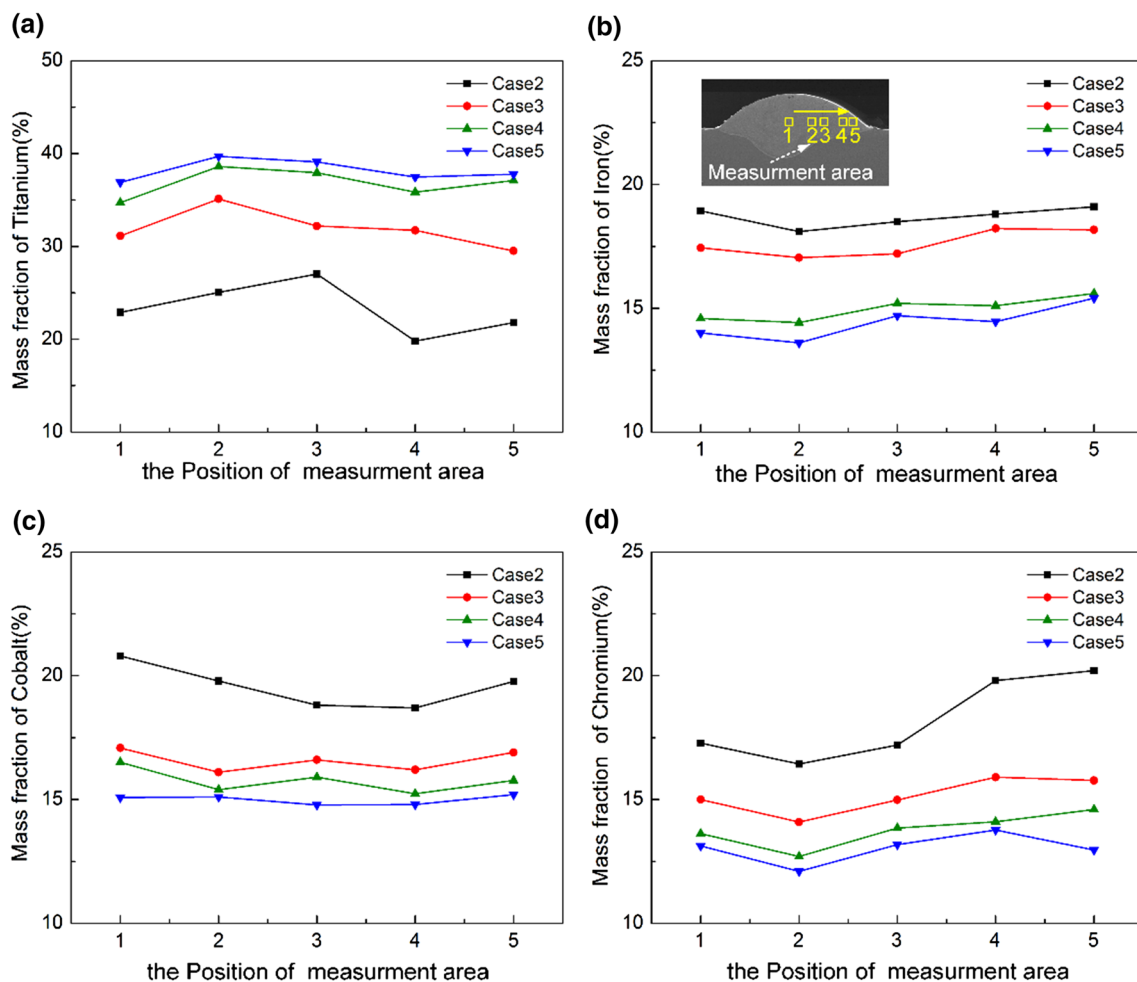


Fig. 16 The element distribution of middle zone in the coating. **a** titanium; **b** iron; **c** cobalt; **d** chromium

Acknowledgements The authors gratefully acknowledge by the Foundation of National Key Laboratory of Science and Technology on Helicopter Transmission (Nanjing University of Aeronautics and Astronautics) (Grant No. HTL-A-19K02).

Compliance with Ethical Standards

Conflict of interest All authors declare that they have no conflict of interest.

References

1. D. Banerjee, J.C. Williams, *Acta Mater.* **61**, 844 (2013)
2. C. Yang, X. Cheng, H. Tang, X. Tian, D. Liu, *Surf. Coat. Technol.* **337**, 97 (2017)
3. D.G. Bansal, O.L. Eryilmaz, P.J. Blau, *Wear* **271**, 2006 (2011)
4. P. Farahmand, R. Kovacevic, *Surf. Coat. Technol.* **276**, 121 (2015)
5. O.S. Adesina, A.P.I. Popoola, S.L. Pityana et al., *Int. J. Adv. Manuf. Technol.* **95**, 1265 (2018)
6. S.R. Al-Sayed Ali, A.H.A. Hussein, A.A.M.S. Nofal, S.E.I. Hasseb Elnaby, H.A. Elgazzar, H.A. Sabour, *Materials* **10**, 1178 (2017)
7. X. Luo, J. Li, G.J. Li, *J. Alloy. Compd.* **626**, 102 (2015)
8. J.M. Chen, C. Guo, J.S. Zhou, T. Nonferr, *Metal. Soc.* **22**, 2171 (2012)
9. J.D. Majumdar, I. Manna, A. Kumar, P. Bhargava, A.K. Nath, *J. Mater. Process. Tech.* **209**, 2237 (2009)
10. L. Jianing, C. Chuanzhong, Z. Lei, *Int. J. Refract. Met. H.* **29**, 49 (2011)
11. J. Li, C. Chen, Z. Lin, T. Squartini, *J. Alloy. Compd.* **509**, 4882 (2011)
12. Y.Q. Yang, H.C. Man, *Surf. Coat. Technol.* **201**, 6928 (2007)
13. Y. Yu, J. Zhou, J. Chen, H. Zhou, C. Guo, L. Wang, L. Yang, *Wear* **274–275**, 298 (2012)
14. L.L. Bai, J. Li, J. Chen, R. Song, J.Z. Shao, C.C. Qu, *Opt. Laser Technol.* **76**, 33 (2016)
15. R. Song, J. Li, J.Z. Shao, L.L. Bai, J.L. Chen, C.C. Qu, *Appl. Surf. Sci.* **355**, 298 (2015)
16. J.Z. Shao, J. Li, R. Song, L.L. Bai, J.L. Chen, C.C. Qu, *Rare Metals* **39**, 304 (2020)
17. M.S. Selamat, L.M. Watson, T.N. Baker, *J. Mater. Process. Tech.* **142**, 725 (2003)
18. C.G. Li, Y. Wang, L. Guo, J. He, Z. Pan, L. Wang, *J. Alloy. Compd.* **506**, 356 (2010)
19. J. Li, Z. Yu, H. Wang, *Thin Solid Films* **519**, 4804 (2011)

20. S. Feng, H.B. Tang, S.Q. Zhang, H.M. Wang, T. Nonferr, *Metal Soc.* **22**, 1667 (2012)
21. J.-W. Yeh, S.-K. Chen, S.-J. Lin, J.-Y. Gan, T.-S. Chin, T.-T. Shun, C.-H. Tsau, S.-Y. Chang, *Adv. Eng. Mater.* **6**, 299 (2004)
22. Y. Ma, Q. Wang, B.B. Jiang, C.L. Li, J.M. Hao, X.N. Li, C. Dong, T.G. Nieh, *Acta Mater.* **147**, 213 (2018)
23. H. Zhang, Y. Pan, Y.Z. He, *Mater. Design* **32**, 1910 (2011)
24. J.Y. He, H. Wang, Y. Wu, X.J. Liu, H.H. Mao, T.G. Nieh, Z.P. Lu, *Intermetallics* **79**, 41 (2016)
25. C. Huang, Y. Zhang, R. Vilar, J. Shen, *Mater. Design* **41**, 338 (2012)
26. H.X. Zhang, J.J. Dai, C.X. Sun, S.Y. Li, *J. Mater. Process. Tech.* **282**, 116671 (2020)
27. M. Guo, S. Chen, F. Shang et al., Laser cladding novel NiCr-SiFeBW–CeO₂ coating with both high wear and corrosion resistance. *Met. Mater. Int.* (2020). <https://doi.org/10.1007/s12540-020-00756-z>
28. G.S. Ham, Y.K. Kim, Y.S. Na et al., Effect of Ti addition on the microstructure and high-temperature oxidation property of AlCo-CrFeNi high-entropy alloy. *Met. Mater. Int.* (2020). <https://doi.org/10.1007/s12540-020-00708-7>
29. T.M. Yue, H. Xie, X. Lin, H.O. Yang, G.H. Meng, *J. Alloy. Compd.* **587**, 588 (2014)
30. G. Jin, Z. Cai, Y. Guan, X. Cui, Z. Liu, Y. Li, M. Dong, D. Zhang, *Appl. Surf. Sci.* **445**, 113 (2018)
31. W.E. King, A.T. Anderson, R.M. Ferencz, N.E. Hodge, C. Kamath, S.A. Khairallah, A.M. Rubenchik, *Appl. Phys. Rev.* **2**, 041304 (2015)
32. A. Sim, E.-J. Chun, D.-W. Cho, *Met. Mater. Int.* **26**, 1207 (2020)
33. P. Campra, D. Millstein, *Environ. Sci. Technol.* **47**, 12284 (2013)
34. Y.Q. Jiang, J. Li, Y.F. Juan, Z.J. Lu, W.L. Ji, *J. Alloy. Compd.* **775**, 1 (2018)
35. S. Guo, C. Ng, J. Lu, C.T. Liu, *J. Appl. Phys.* **109**, 103505 (2011)
36. S.A. Kube, S. Sohn, D. Uhl, A. Datye, A. Mehta, J. Schroers, *Acta Mater.* **166**, 677 (2019)
37. J. Cieslak, J. Tobola, K. Berent, M. Marciszko, *J. Alloy. Compd.* **740**, 264 (2018)
38. C. Zhang, F. Zhang, H. Diao, M.C. Gao, Z. Tang, J.D. Poplawsky, P.K. Liaw, *Mater. Design* **109**, 425 (2016)
39. H.R. Sista, J.W. Newkirk, F.W. Liou, *Mater. Design* **81**, 113 (2015)
40. S. Guo, Q. Hu, C. Ng, C.T. Liu, *Intermetallics* **41**, 96 (2013)
41. H.L. Wei, Y. Cao, W.H. Liao, T.T. Liu, **34**, 101221 (2020).
42. S.A. Khairallah, A.T. Anderson, A. Rubenchik, W.E. King, *Acta Mater.* **108**, 36 (2016)
43. X. Zhan, J. Chen, J. Liu, Y. Wei, J. Zhou, Y. Meng, *Mater. Design* **99**, 449 (2016)

Publisher's Note Springer Nature remains neutral with regard to jurisdictional claims in published maps and institutional affiliations.